J. Fluid Mech. (1999), *vol.* 397, *pp.* 99–117. Printed in the United Kingdom

Interaction of capillary waves with longer waves. Part 2. Applications to waves in two surface dimensions and to waves in shallow water

By KENNETH M. WATSON

Marine Physical Laboratory, Scripps Institution of Oceanography,
University of California at San Diego, CA 92093-0213, USA

(Received 31 July 1998 and in revised form 17 May 1999)

In Part 1 of this work we presented a new mathematical formulation for numerical investigation of capillary wave dynamics. This permitted calculations to be readily performed on a desktop computer. Applications given were primarily to waves in one surface dimension. In Part 2 we describe further applications to waves in two surface dimensions and also to waves in shallow water (not, however, shallow for the capillary waves). Wavenumber–frequency spectra for wind waves are calculated. As was observed in tank experiments by Hara *et al.* (1997), our calculations show both a frequency spread and a frequency up-shifting which suggests that capillary waves are 'dragged along' by longer waves. Fine-scale roughness near wind wave crests shows a transitory nature, changing with the wave pattern. We discuss implications of this for microwave remote sensing. The propagation of short gravity waves in shallow water is studied. As these waves develop bore-like forward faces, generation of parasitic capillary waves is observed. Generation rates for these are substantially greater than observed for waves in deep water.

1. Introduction

In Part 1 of this work (Watson & Buchsbaum 1996) a model was introduced for investigating capillary wave interactions with longer waves. The Hamiltonian formulation of Zakharov (1968), Miles (1977), and Milder (1990) for irrotational flow was used. A modification of the canonical transformation theory of Creamer *et al.* (1989) was developed to substantially simplify numerical calculations. This permits the calculations described to be done on a desktop computer. Viscous dissipation was introduced into the theory as an option that could be turned on or off.

The applications presented in Part 1 were principally to wave systems in one (surface) dimension. The role of three-wave and four-wave resonances was investigated. It was found that in general off-resonance interactions are of major importance.

The radiation of parasitic capillary waves was described by Ebuchi, Kawamura & Toba (1987), Perlin, Lin & Ting (1993), and Longuet-Higgins (1995). Calculations of these phenomena were presented in Part 1.

The generation of capillary waves from a system of wind-driven waves was investigated. It was found that nonlinear interactions extended to shorter wavelengths the spectra of waves generated directly by the wind. The calculation of this effect was motivated by the observations of Cox (1958), Jähne & Riemer (1990), Klinke &

Jähne (1992), Zhang & Cox (1994), and Zhang (1995). The cut-off of the spectra at wavelengths in the range $\frac{1}{3}$ to $\frac{1}{2}$ cm observed by these authors was also seen in the calculations reported in Part 1.

Calculations of the rate at which capillary waves are generated by wind waves were compared to similar calculations (Watson & McBride 1993) using the Hasselmann (1968) radiative transport model. For the cases studied, the Hasselmann model underestimated the generation rates by factors from 2 to 10. This discrepancy was interpreted as due to off-resonance interactions, which are neglected in the Hasselmann theory.

In this paper we present further studies of capillary wave interactions, principally to wave systems in two surface dimensions. Relaxation rates and wavenumber–frequency spectra are investigated. The calculated frequency spread and frequency up-shifting are similar to the observations of Hara, Bock & Donelan (1997). Capillary wave roughness on wind wave surfaces is also described and implications for microwave remote sensing are discussed.

In § 5 we extend our previous studies to investigate parasitic capillary generation by waves in shallow water (not shallow to the parasitic capillaries, however). Freilich & Guza (1984) have observed that the role of three-wave interactions for gravity waves is greatly enhanced in shallow water. We confirm this effect, seeing strong parasitic capillary wave generation from waves with slopes as small as $\frac{1}{5}$ that required for waves in deep water.

2. The wave model

The model used here was described in detail in Part 1. Consequently, we shall now give this only a brief review.

Irrotational, inviscid flow is described by a velocity potential $\Phi(\boldsymbol{x}, z)$. In the rectangular coordinate system used here the undisturbed water surface is at $z = 0$, with points above this surface corresponding to $z > 0$. A horizontal vector is written as $\boldsymbol{x} = (x, y)$. The vertical displacement of the water surface at $\boldsymbol{x}$ is $\zeta(\boldsymbol{x})$. The velocity potential on the water surface is

$$\phi(\boldsymbol{x}) \equiv \Phi(\boldsymbol{x}, \zeta(\boldsymbol{x})). \tag{2.1}$$

Zakharov (1968), Miles (1977), and Watson, West & Cohen (1976) have noted that ϕ and ζ are cononical variables in a Hamiltonian formulation of the wave motion. The Hamiltonian method was used in Part 1, following the work of Milder (1990). Although of course not necessary, the use of Hamilton's equations is a convenience for analytical developments.

As in Part 1, the 'ocean' is confined to a rectangular box of dimensions X and Y, with area $A_0 = XY$. The field amplitudes are Fourier expanded in this area. For example, the vertical displacement of the water surface is then

$$\zeta(\boldsymbol{x}, t) = \sum_{\boldsymbol{k}} 1/(2k)[a_{\boldsymbol{k}} \mathrm{e}^{\mathrm{i}(\boldsymbol{k}\cdot\boldsymbol{x} - \omega_k t)} + \text{c.c.}]. \tag{2.2}$$

Here the discrete wavenumber vectors are of the form

$$\left.\begin{aligned} k_x &= n_x k_{0x}, \quad k_y = n_y k_{0y}, \quad n_x, n_y \text{ integers}, \\ k_{0x} &= \frac{2\pi}{X}, \qquad k_{0y} = \frac{2\pi}{Y}. \end{aligned}\right\} \tag{2.3}$$

The angular frequency for a linear wave of wavenumber k is

$$\omega_k = [k(g + \tau k^2)]^{1/2}. \tag{2.4}$$

Here g is the acceleration due to gravity and

$$\tau = 7.5 \times 10^{-5}\,\mathrm{m^3\,s^{-1}} \tag{2.5}$$

represents a nominal value for the surface tension parameter.

The quantities a_k in (2.2) represent slope amplitudes. For linear inviscid waves these are time independent. When nonlinear interactions are taken into account, they satisfy the first-order coupled differential equations

$$\frac{\mathrm{d}a_{\boldsymbol{k}}}{\mathrm{d}t} + \varepsilon_1[\beta a_{\boldsymbol{k}}] = T_3(\boldsymbol{a}, \boldsymbol{k}) \ldots . \tag{2.6}$$

The 'three-wave' term here is

$$T_3(\boldsymbol{a};\boldsymbol{k}) = -\frac{\mathrm{i}}{8V_k}\sum_{l,p}\frac{k}{lp}\{\delta_{k-l-p}\Gamma(\boldsymbol{k},\boldsymbol{p},\boldsymbol{l})a_{\boldsymbol{l}}a_{\boldsymbol{p}}\mathrm{e}^{\mathrm{i}(\omega_k-\omega_l-\omega_p)t} + 2\delta_{\boldsymbol{k}+\boldsymbol{l}-\boldsymbol{p}}\Gamma(\boldsymbol{p},\boldsymbol{k},\boldsymbol{l})a_{\boldsymbol{p}}a^*_{\boldsymbol{l}}$$

$$\times\mathrm{e}^{\mathrm{i}(\omega_k+\omega_l-\omega_p)t} + \delta_{\boldsymbol{k}+\boldsymbol{l}+\boldsymbol{p}}h(\boldsymbol{l},\boldsymbol{p},\boldsymbol{k})a^*_{\boldsymbol{l}}a^*_{\boldsymbol{p}}\mathrm{e}^{\mathrm{i}(\omega_k+\omega_l+\omega_p)t}\}. \tag{2.7}$$

Here V_k is the phase velocity of a linear wave of wavenumber k and the coefficients Γ and h are given in Part 1 (see also (A 10) in the Appendix). The quantity β above describes viscous damping,

$$\beta = 2\nu k^2, \tag{2.8}$$

where ν is the kinematic viscosity, given here a nominal value of $1.3 \times 10^{-6}\,\mathrm{m^2\,s^{-1}}$.† The coefficient ε_1 in (2.6) is to be taken as zero or unity, depending upon whether we wish to keep damping in our calculations. When $\varepsilon_1 = 0$, energy is conserved and this provides a useful check of numerical accuracy. With $\varepsilon_1 = 1$, the maximum energy loss encountered has been no more than 10%. Most of our calculations have been repeated with and without damping. The calculations presented in §§ 3 and 4 include damping.

The term T_3 in (2.6) is the first of an infinite series of increasing order in the a (Milder 1990). The 'four-wave' term T_4 was included in Part 1, where extensive calculations were made, with and without, this term. For wave systems with small slopes, such as the wind waves considered in this paper, relatively little effect was seen from the four-wave term (see figures 1 and 5 and table 2 of Part 1). For steeper waves, effects from the four-wave term could be identified (see figure 3 of Part 1). In this work we shall not be concerned with waves of large slope and shall neglect the four-wave term.

Since equations (2.6) must be integrated numerically, it is necessary to choose a maximum wavenumber cut-off

$$k_c = \frac{2\pi}{\lambda_c}. \tag{2.9}$$

Then,

$$k \leqslant k_c. \tag{2.10}$$

The observations of Jähne & Riemer (1990) and of Zhang & Cox (1994) suggest that wind-driven capillary spectra have very little energy for wavelengths less than $\frac{1}{2}$ to $\frac{2}{3}$ cm. We shall therefore choose λ_c in this range, except when we discuss parasitic

† The introduction of viscous damping into the Hamiltonian theory was described in Part 1.

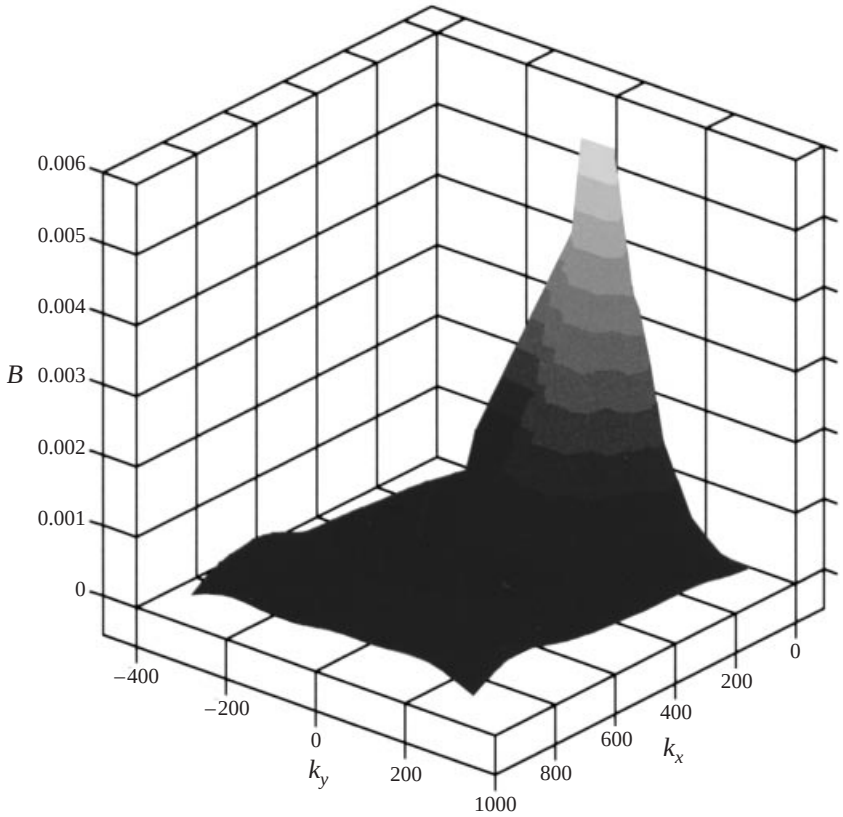

FIGURE 1. Dimensionless wave spectrum (3.13) calculated at time $t = 0.225$ s for the input data (3.14). Units for $\boldsymbol{k}$ are rad m^{-1}.

capillary waves in § 5. Neglecting waves shorter than this was seen in Part 1 to have negligible effect on waves of $\frac{1}{2}$ cm wavelength and longer.

We choose X, Y, and λ_c such that

$$L_x = \frac{X}{\lambda_c}, \quad L_y = \frac{Y}{\lambda_c} \tag{2.11}$$

are integers. We shall consider the positive x-axis as the principal direction of propagation, restricting the wavenumber range (2.3) to

$$1 \leqslant n_x \leqslant M_x = L_x, \quad -M_y \leqslant n_y \leqslant M_y, \tag{2.12}$$

where $M_y \leqslant L_y$. The wavenumbers in (2.6) thus form a finite, discrete set D.

A triad resonance occurs when for a given term in (2.7) the following condition is satisfied:

$$f^{\pm} = |\omega_k \pm \omega_l - \omega_p| < \varepsilon_{res}. \tag{2.13}$$

Here ε_{res} is 'small' – a precise criterion for 'smallness' is not required for our present numerical calculations. It was noted in Part 1 that a necessary condition for a triad resonance to occur is that all three wavenumbers $(\boldsymbol{k}, \boldsymbol{l}, \boldsymbol{p})$ lie in a wavenumber domain D_R. When D_R is a subset of the full wavenumber domain D a canonical transformation technique can be used to integrate (2.6). When this technique is used the only terms

appearing in (2.7) are those for which all three wavenumbers lie in D_R. The use of the canonical transformation has been found to reduce computation times by as much as one or two orders of magnitude. The technique used is a modification of that developed by Creamer *et al.* (1989) and is described in detail in Part 1.

In this work equations (2.6) are initialized by assigning numerical values to the slope amplitudes at time $t = 0$. As in Part 1, when considering wind waves, we assign initial magnitudes using the Donelan–Pierson (1987) spectrum, with a random number generator to provide phases. For other applications specific initial amplitudes may be used.

The numerical calculations reported here were done in double precision on a Macintosh 8500/180 computer. Individual integrations of (2.6) required as much as 2 to 20 minutes.†

3. Relaxation rates and power spectra

For the applications of this section we consider wind waves. As described above, for a given wind speed U_{10} the slope amplitudes in (2.6) are initialized with random phases and magnitudes obtained from the Donelan–Pierson (1987) spectrum. Ensembles are generated by repeating a given calculation, changing only the initial phases. Ensembles consisting of 150 runs were used in this work. Comparisons were made of results using ensembles of 50, 100, and 150 runs. Little difference was seen in the 100 and 150 element ensembles. For 50 run ensembles the weak outlying areas in the power spectra showed some statistical variations.

The triad interactions described by (2.6) are strong and result in fast capillary response times. We shall illustrate this with both auto-correlation decay rates and power spectra.

The auto-correlation function for surface displacement is

$$C(t;\boldsymbol{r},\tau) = \langle \zeta(\boldsymbol{x}+\boldsymbol{r}/2, t+\tau/2)\zeta(\boldsymbol{x}-\boldsymbol{r}/2, t-\tau/2)\rangle, \tag{3.1}$$

where $\langle\cdots\rangle$ represents an ensemble average. Because of the phase averaging, we do not except C to depend on $\boldsymbol{x}$. We see from (3.1) that

$$C(t;\boldsymbol{r},\tau) = C(t;-\boldsymbol{r},-\tau). \tag{3.2}$$

Also, because of the ensemble average over phases, (3.1) takes the form

$$C(t;\boldsymbol{r},\tau) = \sum_{\boldsymbol{p}} \frac{1}{4p^2}[G_{\boldsymbol{p}}(\tau)\mathrm{e}^{\mathrm{i}(\boldsymbol{p}\cdot\boldsymbol{r}-\omega_p\tau)} + \text{c.c.}], \tag{3.3}$$

where

$$G_{\boldsymbol{p}}(\tau) = \langle a_{\boldsymbol{p}} * (t-\tau/2)a_{\boldsymbol{p}}(t+\tau/2)\rangle \tag{3.4}$$

and

$$G_{\boldsymbol{p}}(\tau) = G_{\boldsymbol{p}} * (-\tau). \tag{3.5}$$

Since we are integrating over time with specific initial conditions, we may expect the G to depend also on t.

† Since completing the calculations described here, a coding modification has been found which can significantly reduce computation times.

The power spectrum of the wave system is

$$\hat{P}(\boldsymbol{k},\Omega) = \int \frac{\mathrm{d}^2 r}{A_0} \int \frac{\mathrm{d}\tau}{2\pi} \mathrm{e}^{-\mathrm{i}(\boldsymbol{k}\cdot\boldsymbol{r}-\Omega t)} C(t;\boldsymbol{r},\tau)$$
$$= \hat{P}^*(\boldsymbol{k},\Omega) = \hat{P}(-\boldsymbol{k},-\Omega). \tag{3.6}$$

Normalized to a continuous wavenumber distribution, this spectrum is

$$P(\boldsymbol{k},\Omega) = \frac{1}{k_{0x}k_{0y}} \hat{P}(\boldsymbol{k},\Omega), \tag{3.7}$$

so

$$\int \mathrm{d}^2 k \, \mathrm{d}\Omega \, P(\boldsymbol{k},\Omega) = \langle \zeta^2 \rangle. \tag{3.8}$$

Because of the restriction (2.12) $G_{\boldsymbol{p}}(\tau) = 0$ for $p_x < 0$. Thus, if $k_x > 0$, we have

$$P(\boldsymbol{k},\Omega) = \frac{1}{4k^2 k_{0x} k_{0y}} \int \frac{\mathrm{d}\tau}{2\pi} \mathrm{e}^{\mathrm{i}(\Omega-\omega_k)\tau} G_{\boldsymbol{k}}(\tau). \tag{3.9}$$

We can restrict ourselves to the case $\Omega > 0$ because of the rapidly oscillating exponential. For the domain $k_x < 0$, $\Omega < 0$ and k_y changed in sign, we just duplicate (3.9) (see (3.6)). We therefore lose no information if we restrict ourselves to the domain $k_x > 0$, $\Omega > 0$ and use just (3.9), which should then be multiplied by a factor of 2 if we wish to preserve the normalization (3.8).

The autocorrelation function G may be expressed as

$$G_{\boldsymbol{k}}(\tau) = R_{\boldsymbol{k}}(\tau) + \mathrm{i} I_{\boldsymbol{k}}(\tau), \tag{3.10}$$

where $R_{\boldsymbol{k}}$ and $I_{\boldsymbol{k}}$ are real, and

$$R_{\boldsymbol{k}}(0) = \langle |a_{\boldsymbol{k}}|^2 \rangle, \quad I_{\boldsymbol{k}}(0) = 0. \tag{3.11}$$

Numerical integration of (2.6) extends over the time interval $0 \leqslant t \leqslant T$. The time variables T and t (t appearing implicitly in (3.10)) will be chosen as

$$T = 0.35\,\mathrm{s}, \quad t = 0.225\,\mathrm{s}. \tag{3.12}$$

The dimensionless power spectrum in wavenumber space is

$$B(\boldsymbol{k}) = 2k^4 \int \mathrm{d}\Omega \, P(\boldsymbol{k},\Omega)$$
$$= \frac{k^2}{2k_{0x}k_{0y}} R_{\boldsymbol{k}}(0). \tag{3.13}$$

The factor of 2 is introduced here to account for the domain $k_x < 0$, as mentioned in connection with (3.9). It was seen in Part 1 that the spectrum $B(\boldsymbol{k})$ has a 'cut-off' at wavenumbers $\lambda \approx 0.5\,\mathrm{cm}$, consistent with the observations of Cox (1958), Jähne & Riemer (1990), and Zhang & Cox (1994), and the calculations of Federov & Melville (1998).

We now illustrate the above with our first example:

$$U_{10} = 4\,\mathrm{m\,s^{-1}}, \quad X = Y = 20\,\mathrm{cm}, \quad M_x = 30, \quad M_y = 10. \tag{3.14}$$

We note that for $U_{10} = 4\,\mathrm{m\,s^{-1}}$, the Donelan–Pierson (1987) spectrum has a sharp cut-off at $k \approx 440\,\mathrm{rad\,m^{-1}}$ or $\lambda \approx 1.5\,\mathrm{cm}$. Shorter-wavelength waves are generated by the dynamics.

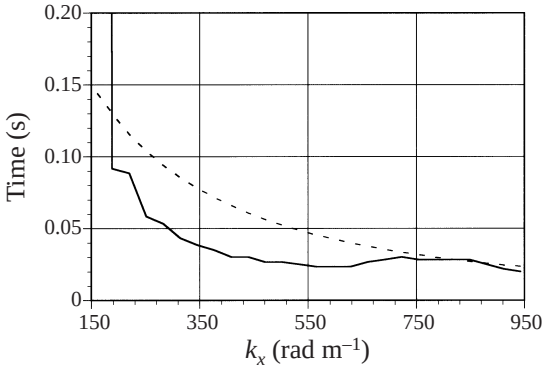

FIGURE 2. Decay time, shown by solid line, for the auto-correlation function R_k to fall to one-half its initial value at zero lag. Data are given by (3.14) and output is on line $k_y = 0$. The dashed line shows the linear wave period.

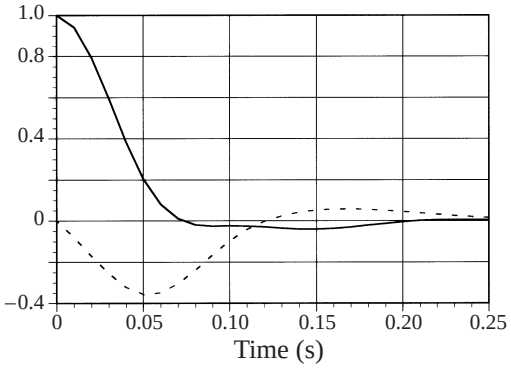

FIGURE 3. The correlation functions R_k (solid line) and I_k (dashed line) are shown for the data (3.14) and $k_x = 785\,\mathrm{rad\,m^{-1}}, k_y = 0$. These quantities have here been normalized by $R_k(0)$.

In figure 1 we show the spectrum B (3.13) for the parameters (3.14) at time $t = 0.225$ s. The spectrum is quite similar at the final time $T = 0.35$ s.

For the parameters (3.14) and for $k_y = 0$, we show in figure 2 the decay time as a function of k_x (the solid curve) for R_k to fall to half its value at $\tau = 0$. Also shown is the linear wave period (as the dashed curve). For wavelengths <2.5 cm the decay time is comparable to, or less, than the linear wave period. In figure 3 we illustrate the correlation functions R_k (solid curve) and I_k (dashed curve) as functions of lag time τ for a wave of 0.8 cm wavelength. The correlation functions in figure 3 have been normalized by $R_k(0)$.

These short relaxation times illustrate the very significant effect on capillary waves of nonlinear interactions with longer waves. They also illustrate why it was found in Part 1 that interactions far off frequency resonance are important. Surface wave relaxation times have played a significant role in the analysis of radar observations of surface wave modulation effects. We shall discuss this in more detail in § 4.

To evaluate the integral (3.9) we arbitrarily extrapolate to times $|\tau| > T_0$ by setting

$$G_k(\tau) = G_k(T_0)\exp\left[-2(|\tau| - T_0)\right], \quad |\tau| > T_0 \equiv 0.25\,\mathrm{s}.$$

This introduces a fine-scale spectral smoothing which is not significant for our spectra.

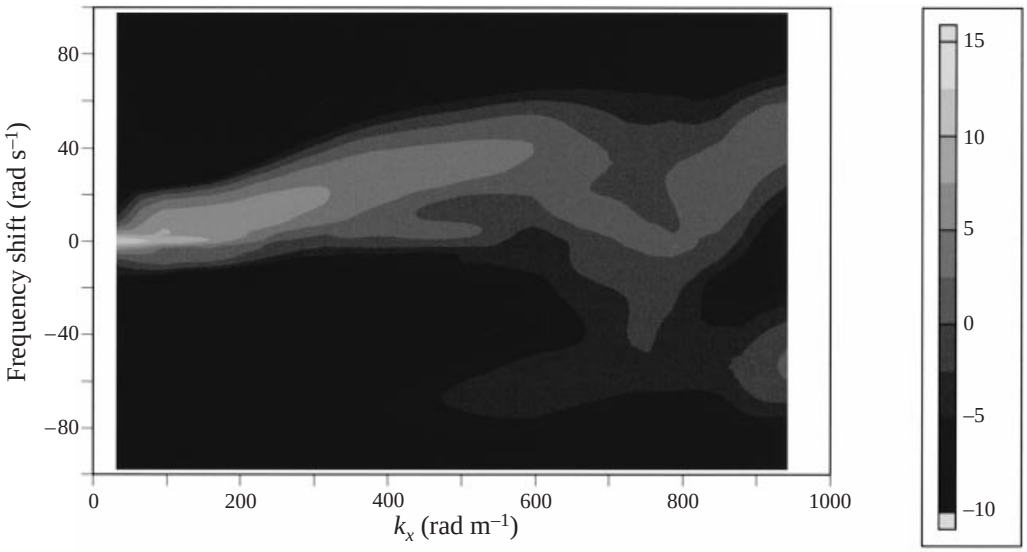

FIGURE 4. The frequency–wavenumber spectrum (3.15). The spectral intensity is shown as a function of the frequency difference $(\Omega - \omega_k)$ and the wavenumber $\boldsymbol{k}$ along the line $k_y = 0$.

For displaying the wavenumber–frequency spectrum the strong variation of B with k seen in figure 1 suggests using the normalized spectrum

$$S(k_x, k_y, \Omega) = 10 + 10 \log \left(\frac{2P(\boldsymbol{k}, \Omega) k^4}{B(\boldsymbol{k})} \right). \tag{3.15}$$

(The factor of 2 here compensates for the corresponding factor in (3.13).) To show (3.15) we use an intensity plot with the frequency difference $(\Omega - \omega_k)$ as ordinate and the wavenumber k (along a straight line in $\boldsymbol{k}$-space) as abscissa. Nearest-neighbour wavenumber smoothing is used in the plots.

In figure 4 we show the spectrum (3.15) for the case (3.14) and along the line $k_y = 0$. For $k < 500\,\mathrm{rad\,m^{-1}}$ there is strong admixture of Donelan–Pierson waves and the linear wave dispersion relation is evident. For $k < 600\,\mathrm{rad\,m^{-1}}$ the spectrum is predominantly shifted to $(\Omega - \omega_k) > 0$, indicating that the short waves are dynamically coupled to longer, faster propagating waves. There is also seen a downshift in frequency at the higher wavenumbers. Such spectral broadening is expected to result from advection by the orbital current of the longer waves.

Hara *et al.* (1997, to henceforth be referenced as HBD) have evaluated k–Ω spectra from their observations of wind-driven waves in a tank. The fetch for their observations was 13 m. The tank was 0.76 m wide and 0.25 m deep. They resolved waves in the wavenumber range $20 < k < 800\,\mathrm{rad\,m^{-1}}$. Their experiment that seems to best match the conditions of our calculation was that with a wind friction velocity of $0.27\,\mathrm{m\,s^{-1}}$. In this case the spectral peak was at a wavelength $\lambda = 12\,\mathrm{cm}$ (whereas our calculation, although having a lower wind velocity, has a spectral peak at $\lambda = 20\,\mathrm{cm}$). It was necessary for HBD to account for an assumed surface current drift of $0.05\,\mathrm{m\,s^{-1}}$. Such a current does not occur for our calculation.

We consider first the HBD case for which $k_y = 0$, as in our figure 4. For $k > 500\,\mathrm{rad\,m^{-1}}$ they observed spectral spreading, which they attribute to longer-wave orbital current advection. We also see this. The two ridges in figure 4 at a frequency

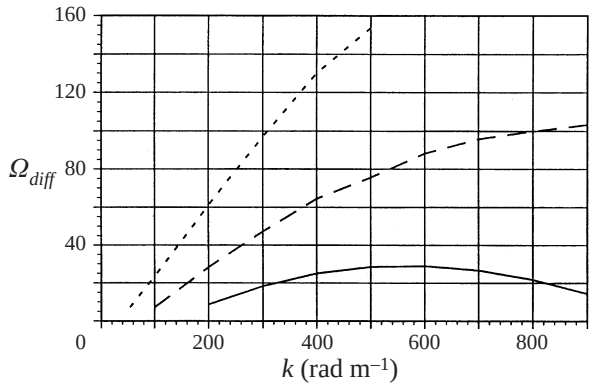

FIGURE 5. The function (3.16) is shown as a function of k for wavelengths $\lambda = 5$ cm (solid curve), 10 cm (long-dashed curve), and 20 cm (short-dashed curve).

shift of ± 50 rad s^{-1} near $k = 900$ rad m^{-1} are consistent with our dominant wave of 20 cm wavelength having a slope of approximately 0.1.

For $k < 500$ rad m^{-1} HBD see two bands. One corresponds to the linear wave dispersion relation. This is seen in our figure 4 along the axis of zero frequency shift. The second band observed by HBD is shifted to frequencies higher than the linear wave frequency. They interpret this as due to short waves 'bound' to longer waves. They observe that for binding to long waves of wavelength λ and phase velocity $c(\lambda)$ the frequency shift should be

$$\Omega_{dif} = c(\lambda)k - \omega_k. \tag{3.16}$$

HBD conclude that their observed frequency shift is consistent with (3.16) for $\lambda = 12$ cm, or 'long waves' at the spectral peak.

In figure 5 we show a plot of the frequency shift (3.16) for long-wave wavelengths of 5 cm (solid curve), 10 cm (long dash curve), and 20 cm (short dash curve). The location of the spectral ridge in figure 4 best matches the curve for $\lambda = 5$ cm in figure 5. The curve for $\lambda = 20$ cm, corresponding to our spectral peak, is displaced well above the ridge in figure 4. If we accept the HBD criterion for waves to be 'bound', we conclude that we have a strong admixture of shorter capillary waves 'bound' to longer waves in the 5–10 cm wavelength range. These waves are somewhat shorter than those found by HBD. We do not have an explanation of this, but recall that their wave spectrum differs from ours and that they appear to have a significant surface drift.

We have noted that the longest wavelength wave contributing to figure 4 is $\lambda = 20$ cm. For an 'ocean' with large fetch waves near the spectral peak at $k \approx g/U_{10}^2$ will modify the capillary spectrum. We can take account of this, as described in Part 1 (§ 5.3). To do this the area $A_0 = XY$ is considered embedded in a much larger area and the canonical transformation technique is used to integrate (2.6) in this large area. The resulting spectrum is shown in figure 6. The spectrum of figure 4 is seen to be much broadened by the orbital currents of much longer waves. The up-shifting of the wave frequency can be seen in figure 6, but this is dominated by the general spectral broadening.

In figure 7 we show the spectrum (3.15) along the 45° line $k_x = k_y$. The up-shifting of wave frequency above the linear wave dispersion line is again seen, but

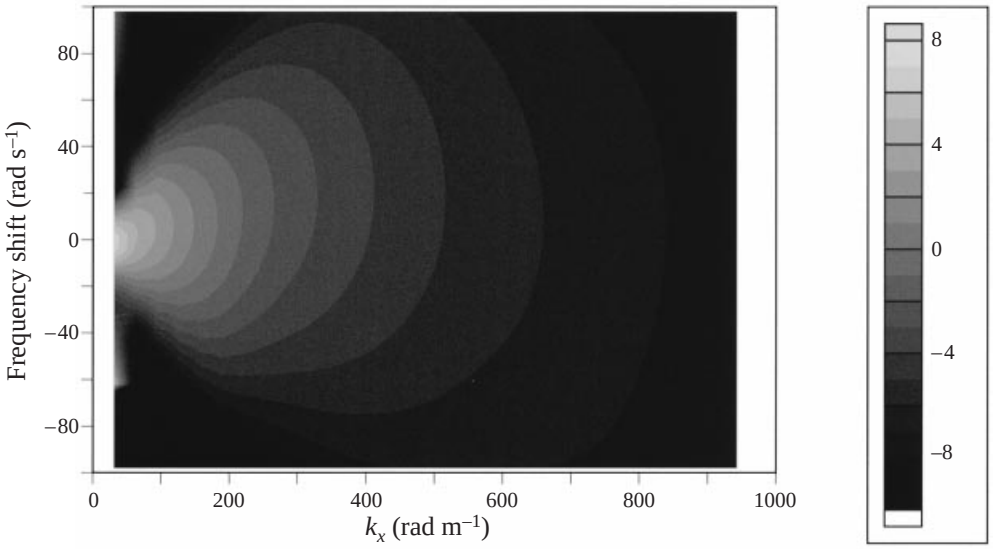

FIGURE 6. The frequency–wavenumber spectrum, as in figure 4, except that interaction is extended to the full wind-wave spectrum.

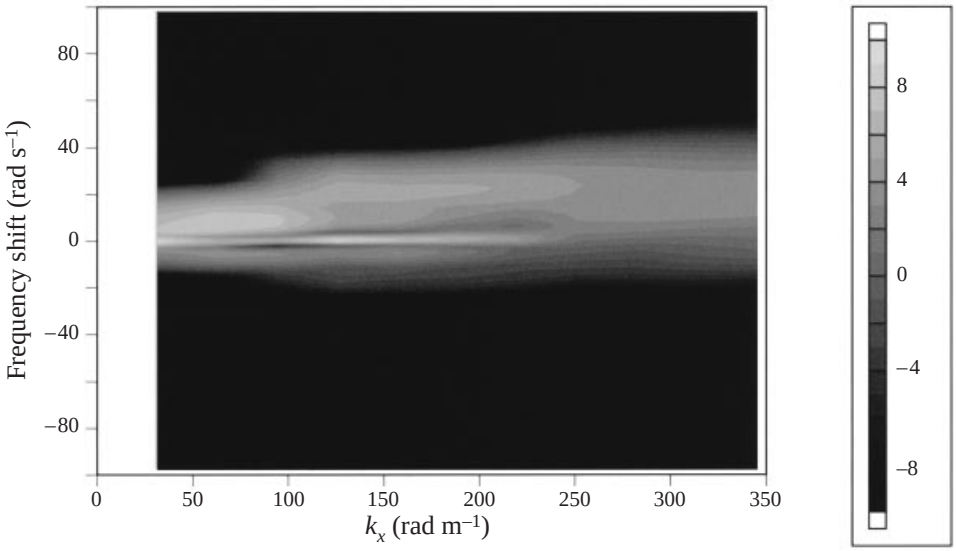

FIGURE 7. The frequency–wavenumber spectrum is plotted as in figure 4, but along the curve $k_y = k_x$.

is less pronounced, and the linear wave dispersion relation is more evident. Similar observations were made by HBD from their data along the 45° line in $\boldsymbol{k}$-space.

We consider a second example, which differs from (3.14) only in that the wind speed is increased:

$$U_{10} = 6\,\mathrm{m\,s^{-1}}, \quad X = Y = 20\,\mathrm{cm}, \quad M_x = 30, \quad M_y = 10. \tag{3.17}$$

For this wind speed the Donelan–Pierson (1987) cut-off is at $k \approx 730\,\mathrm{rad\,m^{-1}}$, or $\lambda \approx 0.9\,\mathrm{cm}$.

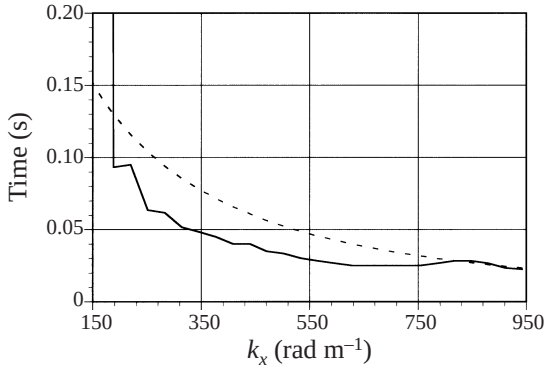

FIGURE 8. The decay time and linear wave period as in figure 2, except that the wind speed is 6 m s^{-1} (see (3.17)).

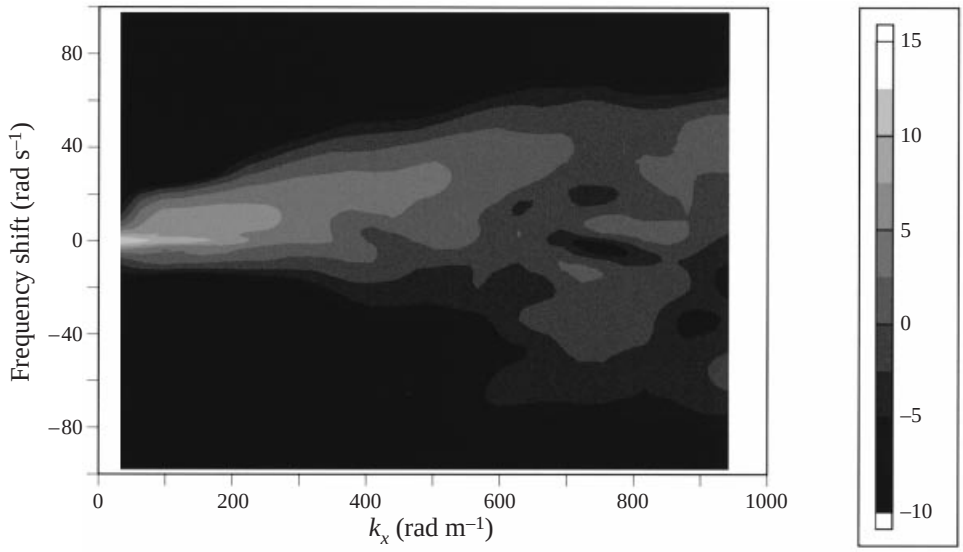

FIGURE 9. The frequency–wavenumber spectrum as in figure 4, except that the wind speed is 6 m s^{-1} (see (3.17)).

In figure 8 we show the decay time (solid line) for this second example and the linear wave period (dashed line). The decay time is very similar to that of figure 2. The frequency–wavenumber spectrum for $k_y = 0$ is shown in figure 9. This does not appear to be significantly different from that of figure 4. Using the HBD interpretation for 'bound' waves, we again conclude that the 'binding' is to waves in the 5–10 cm wavelength range.

4. Modulation of short waves by longer waves

In the last Section we saw that the capillary frequency spectrum was up-shifted, indicating a tendency for the shorter waves to be 'dragged along' by the longer waves. The phase speed was not high enough, however, to imply that these short waves were 'bound' to the longest waves ($\lambda = 20$ cm) at the spectral peak. In this Section we show

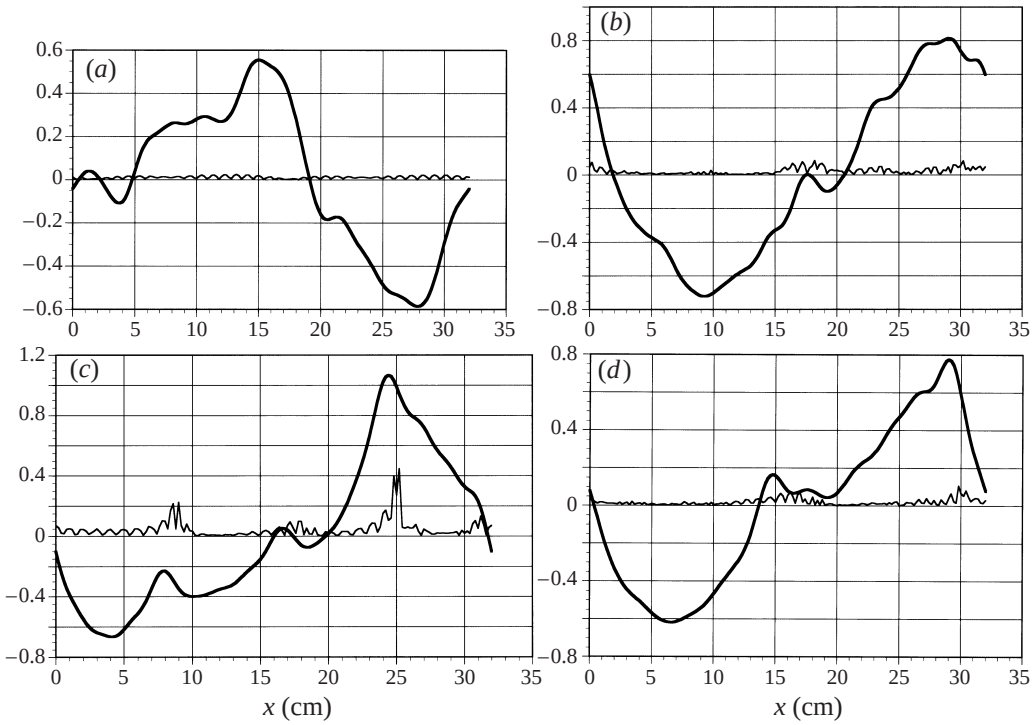

FIGURE 10. The surface displacement in cm (heavy line) and twice the magnitude of the wave slope (light line) as a function of position x. The displacement is filtered, the filter passing wavelengths only in the range $32 \geqslant \lambda > 2$ cm. The slope is also filtered, the filter passing wavelengths only in the range $2 \geqslant \lambda \geqslant 0.4$ cm. (*a*) time $t = 0$, $y = 8$ cm; (*b*) $t = 0.2$ s, $y = 3$ cm; (*c*) $t = 0.2$ s, $y = 8$ cm; (*d*) $t = 0.2$ s, $y = 13$ cm. The wind speed is 4 m s^{-1}.

that although they may not be bound, the capillary waves are strongly modulated by the longer waves and that this has implications for microwave remote sensing.

The first specific example that we shall use to demonstrate this begins at time $t = 0$ with a specific realization of the linear wave field obtained from the Donelan–Pierson (1987) spectrum and the choice of parameters

$$U_{10} = 4\,\mathrm{m\,s^{-1}}, \quad X = 32\,\mathrm{cm}, \quad Y = 16\,\mathrm{cm}, \quad M_x = 80, \quad M_y = 6, \quad 0 \leqslant t \leqslant T = 1\,\mathrm{s} \tag{4.1}$$

To display the output we show the wave displacement ζ filtered to include only wavelengths in the range $32 \geqslant \lambda > 2$ cm. The slope is also filtered to include only wavelengths in the range $2 \geqslant \lambda \geqslant 0.4$ cm. In figures 10 and 11 the surface displacement in cm is shown as the heavy line. The light line shows the magnitude of the slope multiplied by a factor of 2 (in order to more easily read the scale):

$$2\sqrt{(\nabla\zeta)^2}.$$

Displacement and slope for the conditions (4.1) are shown in figure 10. In figure 10(*a*) we show the Donelan–Pierson (1987) input at time $t = 0$ along a cut in the (x, y)-plane at $y = 8$ cm. We note that there is little wave energy in the range $2 \geqslant \lambda \geqslant 0.4$ cm. Figure 10(b, c, d) shows the displacement and slope at $t = 0.2$ s along cuts at $y = 3, 8$, and 13 cm, respectively. Bursts of capillary excitation are evident. These bursts are

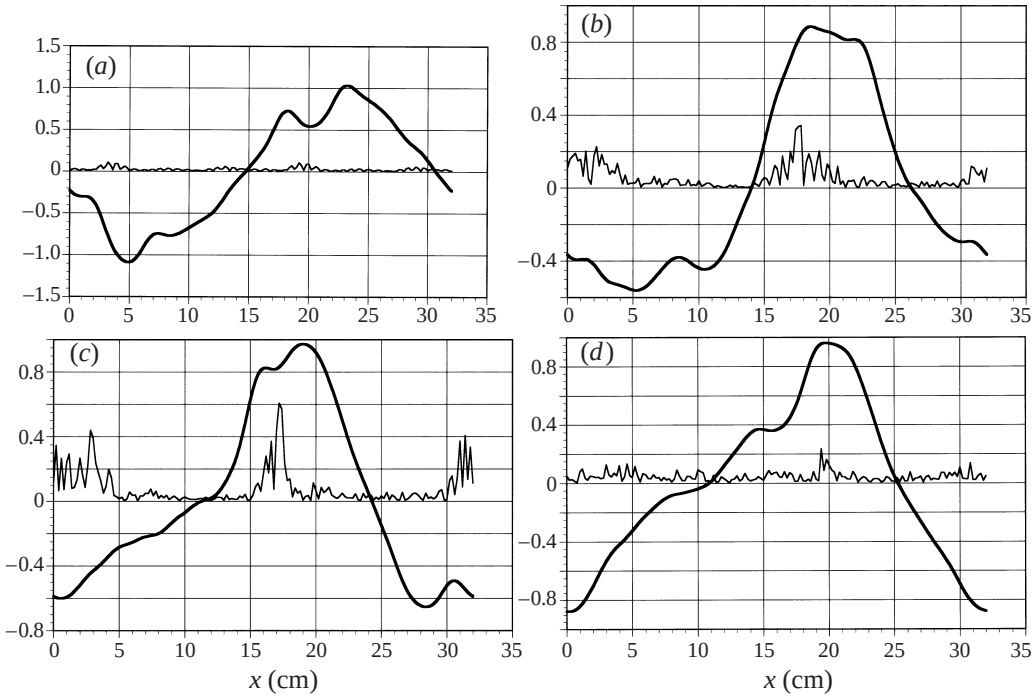

FIGURE 11. Same as figure 10, except that the wind speed is $6\,\mathrm{m\,s^{-1}}$ and the time for (b, c, d) is $t = 0.4\,\mathrm{s}$.

localized in x and y. They are transient phenomena and appear and disappear over the 1 s interval of integration of (2.6). In figure 10 the bursts seem to be generated at wave crests having large curvature and they seem to be shifted somewhat to the forward face of the waves.

The steepest slopes of the curves for displacement in figure 10 are in the range 0.1 to 0.2. This is somewhat less than that which seemed to be required to produce the shorter parasitic capillary waves described in Part 1 and in the work of Longuet-Higgins (1996) and Federov, Melville & Rozenberg (1998).

For the calculations shown in figure 11 we choose the wind speed to be $U_{10} = 6\,\mathrm{m\,s^{-1}}$, otherwise keeping the conditions (4.1). In figure 11(a) we see the Donelan–Pierson (1987) input at time $t = 0$ along the cut at $y = 8\,\mathrm{cm}$. The level of excitation of waves in the range $2 \geqslant \lambda \geqslant 0.4\,\mathrm{cm}$ is greater than was seen in figure 10(a) because of the increased wind speed. Since this is one realization of a Gaussian system the slope amplitude variations seen in figure 11(a) are not correlated with the longer waves. In figure 11(b, c, d) we see the filtered surface displacement and slope at time $t = 0.4\,\mathrm{s}$ along cuts at $y = 3, 8, 13\,\mathrm{cm}$, respectively. We again see bursts of capillary wave exicitation. These are similar to those seen for the case of $4\,\mathrm{m\,s^{-1}}$ wind speed. The amplitudes are now somewhat higher and the bursts are less clearly shifted forward of the crests.

The two data samples shown in figures 10 and 11 were chosen to illustrate that the relation between capillary bursts and wave profile is variable. Over the 1 s integration interval (particularly at $U_{10} = 4\,\mathrm{m\,s^{-1}}$) there were periods of weak burst activity.

Capillary waves in the range $2 \geqslant \lambda \geqslant 0.4\,\mathrm{cm}$ act as Bragg scatterers for X-band and higher-frequency microwave scattering. Excitation and relaxation times have

played an important role in the analysis of observations of surface wave modulation effects. In both the JOWIP (see, for example, Hughes & Dawson 1988) and SARSEX (see, for example, Gasparovic, Apel & Kasischke 1989) experiments detailed studies of the modulation of surface waves by internal waves were made with both *in situ* measurements and radar observations at L-band (approximately 1 GHz) and at X-band (approximately 10 GHz). Agreement between observations and theory was deemed satisfactory for the L-band data (Bragg waves of about 30 cm wavelength). The observed X-band modulation was comparable to that at L-band and about an order of magnitude larger than predicted by calculations (Caponi *et al.* 1988 and Thompson, Gotwols & Sterner 1988). This discrepancy resulted from the short relaxation time expected for the X-band Bragg waves (our even shorter relaxation times shown in figures 2 and 8 would increase this discrepancy).

To explain the X-band discrepancy Caponi *et al.* (1988) and Thompson *et al.* (1988) suggested the 'long-wave effect' that had been proposed earlier by Alpers, Ross & Rufenach (1981). This effect was thought to cause the short Bragg waves to be modulated by longer waves, which in turn were modulated by the internal wave surface currents. An adequate theory of this was not available, however.

Our present model of wave interactions permits us to carry out a calculation of the *long-wave effect*. To do this we shall suppose the system (4.1) to be illuminated by a radar, as in a wave tank experiment.† For a given realization of the initial waves we can calculate radar backscatter when we assign different levels of modulation to the longer waves.

The backscatter amplitude f_R for the electromagnetic wave can be written in the form‡

$$f_R = C \int T(\boldsymbol{x} - \boldsymbol{x}_0) \mathrm{e}^{-\mathrm{i}\boldsymbol{Q}\cdot\boldsymbol{x}} \zeta(\boldsymbol{x}) \, \mathrm{d}^2 x. \tag{4.2}$$

Here $\boldsymbol{Q}$ is the wavenumber of the Bragg wave, assumed to be parallel to the x-axis, T represents the illumination pattern of the radar beam on the water surface, and C is a factor depending on incidence angle, polarization, etc.

For T we shall assume a simple rectangular pattern:

$$\begin{aligned} T(\boldsymbol{x}) &= 1 \quad \text{for } 8 < x < 24, -8 < y < 8 \\ &= 0 \quad \text{otherwise.} \end{aligned} \tag{4.3}$$

The illuminated area is therefore

$$A_R = (16)^2 \, \mathrm{cm}^2. \tag{4.4}$$

The radar cross-section per unit area is then

$$\Sigma = \left\langle \frac{4\pi}{A_R} |f_R|^2 \right\rangle. \tag{4.5}$$

An average over a sequence of observations is implied here.

We shall use a simple model to represent modulation. For a given realization of the initial wave system we shall apply a sequence of modulation factors that multiply all wave amplitudes in the range $32 \geqslant \lambda > 2$ cm by a factor η. Shorter waves are left

† To model radar scattering in a larger area, we would use the canonical transformation technique as was described in connection with figure 6.

‡ The expression (4.2) is equivalent to that used, for example, by Donelan & Pierson (1987) when large amplitude waves of greater wavelength are not present. In this case the 'two-scale' model reduces to (4.2).

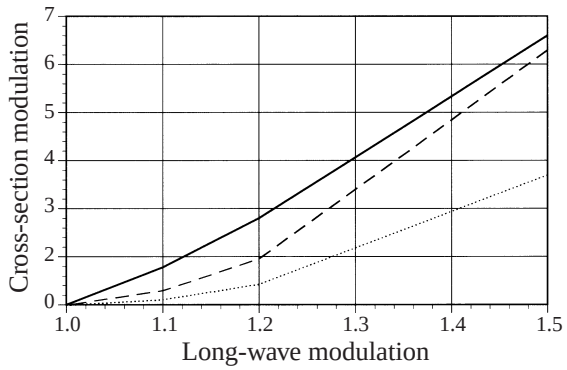

FIGURE 12. The radar modulation (4.6) is shown as a function of the long-wave modulation factor η for Bragg wavelengths of 2 cm (solid curve), $\frac{4}{3}$ cm (dashed curve) and 1 cm (dotted curve).

unchanged. We then integrate (2.6) and average over the interval $0 < t < T = 1$ s for each of the sequence of values for η, beginning with $\eta = 1$. The radar modulation is then

$$M_R(\eta) = \frac{\Sigma(\eta)}{\Sigma(1)}. \tag{4.6}$$

In figure 12 we show the modulation (4.6) as a function of η for Bragg wavelengths of 1, 4/3, and 2 cm. We see, indeed, a very definite long-wave effect. The Bragg waves are significantly modulated by the modulation applied to the longer waves.

A detailed analysis of radar observations of surface wave modulation is beyond our present scope. We have presented the above idealized calculation to show that the long-wave effect, as proposed by Alpers *et al.* (1981), is real and is significant for understanding the response of capillary waves to surface wave modulation. (Note, however, that for their calculation Alpers *et al.* (1981) used the Hasselmann (1968) theory. This technique is inadequate for this purpose and underestimated the effect.)

5. Waves in shallow water

In this Section we investigate the excitation of capillary waves by waves in shallow water. Freilich & Guza (1984) have observed that the role of triad interactions for gravity waves is greatly enhanced when the water is shallow. Their studies suggest that capillary wave excitation may also be sensitive to water depth.

The Hamiltonian formulation of Miles (1977) is valid for water of finite depth, so modification of the deep water theory is straightforward. The linear wave dispersion relation is now

$$\omega_k = [k(g + \tau k^2) \tanh(kD)]^{1/2}, \tag{5.1}$$

where D is the water depth. Equations (2.6) and (2.7) are unchanged in form, except for a modification of the coefficients Γ and h and for the use of (5.1). This is described in the Appendix.

In this Section we shall consider waves in only one surface dimension. For our examples, we choose the cut-off wavelength to be

$$\lambda_c = 0.2\,\text{cm}, \tag{5.2}$$

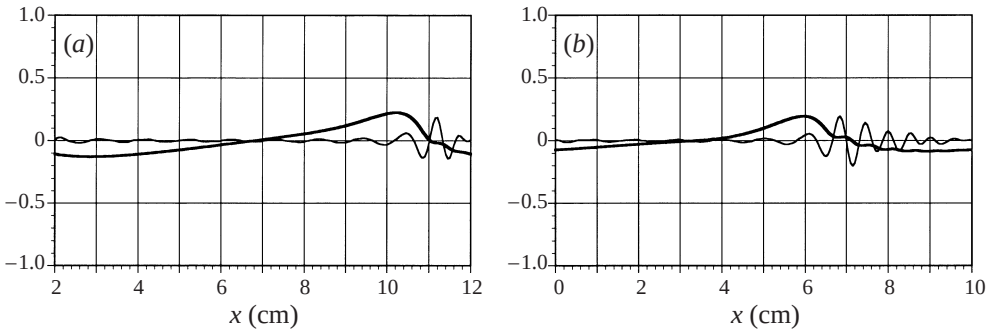

FIGURE 13. Displacement in cm (heavy line) and filtered slope (light line) in the range $1 \geqslant \lambda \geqslant 0.2$ cm. The water depth is 1 cm. (*a*) The initial sine wave slope is 0.1, and the time is $t = 0.3$ s, (*b*) the initial sine wave slope is 0.075 and the time is $t = 0.5$ s.

with a fetch

$$X = 10\,\text{cm}. \tag{5.3}$$

To specify the mode set (2.12) we choose

$$M_x = L_x = 50, \quad M_y = 0. \tag{5.4}$$

The Y-scale need not be specified for calculations in one dimension, but is conveniently chosen as $Y = 1$.

We begin the calculation at time $t = 0$ with a pure sine wave of wavelength 10 cm. The wave amplitude ζ and slope are evaluated for subsequent times. The slope is output through a filter that passes only waves in the range $1 \geqslant \lambda \geqslant 0.2$ cm. The calculations were done with and without dissipation (i.e. $\varepsilon_1 = 0$ or $\varepsilon_1 = 1$ in (2.6)). The effect of dissipation was negligible in our plotted results, so we show these only for the case of no dissipation.

For our first example the initial slope of the sine wave was 0.1 and the water depth $D = 1$ cm. We display the wave amplitude with a heavy line and the slope with a light line in figure 13(*a*) at the time $t = 0.3$ s. The sine wave has developed a bore-like forward face as expected for such a shallow water wave. Short-wavelength capillary waves have developed on the forward face of the longer wave.

For a 10 cm wave in deep water the minimum required slope for such parasitic capillary wave generation is about 0.25 (Longuet-Higgins 1995; Part 1; Federov *et al.* 1998). This confirms the expected enhanced generation of capillary waves in shallow water. The dominant wavelength for the capillary waves in figure 13 is approximately 0.5 cm, comparable to the 0.4 cm wavelength seen by Federov & Melville (1998) for 10 cm deep water waves.

For our second example we again take $D = 1$ cm and an initial sine wave slope of 0.075. The wave displacement and filtered slope profiles are shown at time $t = 0.5$ s in figure 13(*b*). Because of the later time here, the capillary wave system is more fully developed than was the case in figure 13(*a*). The dominant capillary wavelength is approximately 0.5 cm, as before. For our third example (not shown) with an initial sine wave of slope 0.05 and at time 0.5 s, the parasitic capillary waves are weak, with slopes of about 0.01.

Repeating the above calculations for a depth of 2 cm showed capillary wave generation at a reduced rate. For a depth of 5 cm no capillary wave generation was seen for the small initial slopes assumed here.

6. Conclusions

We have provided a formulation of the equations for irrotational wave dynamics which permits one to make rather elaborate calculations on a desktop computer. Using this model, we have investigated the development of wind-wave spectra to short wavelengths. A 'cut-off' for wavelengths of less than about $\frac{1}{2}$ cm was observed. The calculated wavenumber–frequency spectra for wind waves at short wavelengths shows both a spectral broadening and a frequency up-shift, as was observed in tank experiments by Hara *et al.* (1997). Calculations of surface roughness for wind waves show that this is related to the instantaneous surface profile of the longer waves. The level of fine-scale roughness is sensitive to the amplitude of the longer waves, which has implications for microwave remote sensing.

The role of three-wave and four-wave resonances has been studied. For the case of capillary wave interactions the four-wave interactions play a secondary role. However, off-resonance interactions were found to be quite important. This phenomenon was interpreted as limiting the accuracy of kinetic equations that keep only interactions at exact resonance.

We have demonstrated that effects of finite depth can significantly enhance the generation of parasitic capillary waves by longer waves. This investigation was motivated by the work of Freilich & Guza (1984). The mechanism by which the enhancement occurs is not known to us, however.

Partial support for this work was received from the Office of Naval Research Grant N000014-94-1-0013.

Appendix. Wave equations for shallow water

The analysis for waves in deep water, as given in Part 1, needs only minor modification for water of finite depth. We briefly outline this here.

For water of depth D the velocity potential has the form

$$\Phi(\boldsymbol{x}, z) = \sum_{\boldsymbol{k}} C(\boldsymbol{k}, t) \cosh\,[k(z + D)] \mathrm{e}^{\mathrm{i}\boldsymbol{k}\cdot\boldsymbol{x}}, \tag{A 1}$$

where C is a Fourier coefficient. The potential $\phi(\boldsymbol{x}, t)$ at the surface is defined by (2.1). The Hamiltonian is given, for example, by Miles (1977). The expansion of the Hamiltonian in terms of increasing order in the field variables is described by Milder (1990). To third order the Hamiltonian has the form

$$H = H_0 + H_1, \tag{A 2}$$

where

$$\left.\begin{aligned} H_0 &= \tfrac{1}{2}\int [\phi \hat{k} \Lambda \phi + g\zeta^2 + \tau(\nabla\zeta)^2]\, \mathrm{d}^2x, \\ H_1 &= \tfrac{1}{2}\int \zeta [(\nabla\phi)^2 - (\Lambda \hat{k}\phi)^2]\, \mathrm{d}^2x. \end{aligned}\right\} \tag{A 3}$$

Here $\hat{k}$ is the operator satisfying

$$\hat{k}\mathrm{e}^{\mathrm{i}\boldsymbol{k}\cdot\boldsymbol{x}} = k\mathrm{e}^{\mathrm{i}\boldsymbol{k}\cdot\boldsymbol{x}} \tag{A 4}$$

and

$$\Lambda = \tanh\,(D\hat{k}). \tag{A 5}$$

To obtain the equations of motion for the mode amplitudes we expand ϕ and ζ in terms of the *action amplitudes* b_k (see Part 1 for details):

$$\left.\begin{aligned}\phi(\boldsymbol{x},t) &= \sum_{\boldsymbol{k}}(\mu_k/(2A_0))^{1/2}[b_{\boldsymbol{k}}\mathrm{e}^{\mathrm{i}\boldsymbol{k}\cdot\boldsymbol{x}} + \text{c.c.}],\\ \zeta(\boldsymbol{x},t) &= \sum \mathrm{i}/(2A_0\mu_k)^{1/2}[b_{\boldsymbol{k}}\mathrm{e}^{\mathrm{i}\boldsymbol{k}\cdot\boldsymbol{x}} - \text{c.c.}].\end{aligned}\right\} \tag{A 6}$$

Here $A_0 = XY$ and

$$\mu_k = (g + \tau k^2)/\omega_k. \tag{A 7}$$

The equations of motion are (see (2.14) of Part 1)

$$\dot{b}_k = -\mathrm{i}\frac{\partial H}{\partial b_k^*}. \tag{A 8}$$

We can express these equations in terms of the slope amplitudes $a_{\boldsymbol{k}}$ using the relation (see (2.19) of Part 1)

$$b_k = -\mathrm{i}(A_0\mu_k/2)^{1/2}a_k\mathrm{e}^{-\mathrm{i}\omega_k t}/k. \tag{A 9}$$

The equations of motion (2.6) are unchanged in form, except that now the coefficients Γ and h are modified. Only Γ is needed here, which now takes the form

$$\begin{aligned}\Gamma(\boldsymbol{k},\boldsymbol{p},\boldsymbol{l}) = (\omega_k\omega_p)/(kp)[\boldsymbol{k}\cdot\boldsymbol{p}/(\Lambda_k\Lambda_p) - kp] + (\omega_k\omega_l)/(kl)[\boldsymbol{k}\cdot\boldsymbol{l}/(\Lambda_k\Lambda_l) - kl]\\ +(\omega_p\omega_l)/(pl)[\boldsymbol{p}\cdot\boldsymbol{l}/(\Lambda_p\Lambda_l) + pl].\end{aligned} \tag{A 10}$$

Here $\Lambda_k = \tanh(kD)$, etc.

REFERENCES

Alpers, W. R., Ross, D. B. & Rufenach, C. L. 1981 On the detectability of ocean surface waves by real and synthetic aperture radar. *J. Geophys. Res.* **86**, 6481–6498.

Caponi, E. A., Crawford, D. R., Yuen, H. C. & Saffman, P. G. 1988 Modulation of Radar backscatter from the ocean by a variable surface current. *J. Geophys. Res.* **93**, 12249–12264.

Cox, C. S. 1958 Measurements of slopes of high-frequency wind waves. *J. Mar. Res.* **16**, 199–225.

Creamer, D., Henyey, F., Schult, R. & Wright, J. 1989 Improved linear representation of ocean surface waves. *J. Fluid Mech.* **205**, 135–161.

Donelan, M. & Pierson, W. 1987 Radar scattering and equilibrium ranges in wind-generated waves with applications to scatterometry. *J. Geophys. Res.* **92**, 4971–5030.

Ebuchi, N., Kawamura, H. & Toba, Y. 1987 Fine structure of laboratory wind-wave surfaces studied using optical methods. *Boundary-Layer Met.* **39**, 133–151.

Federov, A. & Melville, W. K. 1998 Nonlinear gravity-capillary waves with forcing and dissipation. *J. Fluid Mech.* **354**, 1–42.

Federov, A., Melville, W. K. & Rozenberg, A. 1998 An experimental and numerical study of parasitic capillary waves. *Phys. Fluids* **10**, 1315–1323.

Freilich, M. H. & Guza, R. T. 1984 Nonlinear effects on shoaling surface gravity waves. *Phil. Trans. R. Soc. Lond.* A **311**, 1–41.

Gasparovic, R. F., Apel, J. R. & Kasischke, E. S. 1989 An overview of the SAR Internal Wave Signature Experiment. *J. Geophys. Res.* **93**, 12304–12316.

Hara, T., Bock, E. J. & Donelan, M. 1997 Frequency–wavenumber spectrum of wind generated gravity-capillary waves. *J. Geophys. Res.* **102**, 1061–1072 (referred to herein as HBD).

Hasselmann, K. 1968 Weak-interaction theory of ocean waves. In *Basic Developments in Fluid Mechanics* (ed. M. Holt), pp. 117–182. Academic.

Hughes, B. A. & Dawson, T. W. 1988 Joint Canada-U.S. Ocean Wave Investigation Project: An overview of the Georgia Strait Experiment. *J. Geophys. Res.* **93**, 12219–12234.

JÄHNE, B. & RIEMER, K. 1990 Two-dimensional wave number spectra of small scale water surface waves. *J. Geophys. Res.* **95**, 11531–11546.

KLINKE, J. & JÄHNE, B. 1992 2D wave number spectra of short wind waves – results from wind wave facilities and extrapolation to the ocean. In *Optics of the Air-Sea Interface: Theory and Measurements. Proc. SPIE* 1749, pp. 1–13. Inst. Soc. Opt. Engng.

LONGUET-HIGGINS, M. S. 1995 Parasitic capillary waves: a direct calculation. *J. Fluid Mech.* **301**, 79–107.

MILDER, D. M. 1990 The effects of truncation on surface-wave Hamiltonians. *J. Fluid Mech.* **217**, 249–262.

MILES, J. W. 1977 On Hamilton's principle for surface waves. *J. Fluid Mech.* **83**, 153–164.

PERLIN, M., LIN, H. & TING, C.-L. 1993 On parasitic capillary waves generated by steep gravity waves: an experimental investigation with spatial and temporal measurements. *J. Fluid Mech.* **255**, 597–620.

THOMPSON, D. R., GOTWOLS, B. L. & STERNER II, R. E. 1988 A comparison of measured surface wave spectral modulation with predictions from a wave-current model. *J. Geophys. Res.* **93**, 12334–12339.

WATSON, K., WEST, B. & COHEN, B. 1976 Coupling of surface and internal waves: a mode coupling model. *J. Fluid Mech.* **77**, 185–208.

WATSON, K. M. & BUCHSBAUM, S. B. 1996 Interaction of capillary waves with longer waves. Part 1. General theory and specific applications to waves in one dimension. *J. Fluid Mech.* **321**, 87–120.

WATSON, K. M. & MCBRIDE, J. B. 1993 Excitation of capillary waves by longer waves. *J. Fluid Mech.* **250**, 103–119.

ZAKHAROV, V. E. 1968 Stability of periodic waves of finite amplitude on the surface of deep fluid. *J. Appl. Mech. Tech Phys.* (English transl.) **2**, 190–194.

ZHANG, X. 1995 Capillary-gravity and capillary waves generated in a wind wave tank: observations and theories. *J. Fluid Mech.* **289**, 51–82.

ZHANG, X. & COX, C. S. 1994 Measuring the two-dimensional structure of a wavy water wave surface optically: a surface gradient detector. *Exps. Fluids* **17**, 225–237.